

ORIGINAL ARTICLE

Open Access



General Kinetostatic Modeling and Deformation Analysis of a Two-Module Rod-Driven Continuum Robot with Friction Considered

Peiyi Wang¹, Xinhua Yang¹, Xiangyang Wang² and Sheng Guo^{1*} 

Abstract

Continuum robots actuated by flexible rods have large potential applications, such as detection and operation tasks in confined environments, since the push and pull actuation of flexible rods withstand tension and compressive force, and increase the structure's rigidity. In this paper, a generalized kinetostatics model for multi-module and multi-segment continuum robots considering the effect of friction based on the Cosserat rod theory is established. Then, the model is applied to a two-module rod-driven continuum robot with winding ropes to analyze its deformation and load characteristics. Four different in-plane configurations under the external load term as S1, S2, C1, and C2 are defined. Taking a bending plane as an example, the tip deformation along the x-axis of these shapes is simulated and compared, which shows that the load capacity of C1 and C2 is generally larger than that of S1 and S2. Furthermore, the deformation experiments and simulations show that the maximum error ratio without external loads relative to the total length is no more than 3%, and it is no more than 4.7% under the external load. The established kinetostatics model is proven sufficient to accurately analyze the rod-driven continuum robot with the consideration of internal friction.

Keywords Rod-driven continuum robot, Kinetostatic model, Cosserat rod theory, Deformation and stiffness analysis

1 Introduction

A slender continuum robot possesses a continuous body exhibiting infinitely degree of freedoms, which is unlike those traditional rigid body robots [1, 2]. With a large slenderness ratio body, they can perform operation tasks with various end-effectors in confined and unstructured

space, such as in-suit aeroengine maintenance [3–5], deep cavities [6–8], and medical surgery [9, 10].

To date, numerous continuum robots have been designed. Pneumatic driven continuum robots [11, 12] utilize three or more three parallel pneumatic “muscles” to achieve spatial bending. Several serial-parallel pneumatic “muscles” [13] have a large load capacity by adaptive envelop grasp. Concentric-tube continuum robots [14, 15] are composed of concentric pre-curved elastic tubes. The coupling effect of all internal tubes controls the robot's shape. The most common are tendon-driven continuum robots [16–18] where a flexible backbone is actuated by cabling along the robot's length. As mentioned in Refs. [19, 20], several parallel flexible cables are replaced by rigid links in traditional rigid-link robots. However, cable only provides pulling force and has low

*Correspondence:

Sheng Guo
shguo@bjtu.edu.cn

¹ School of Mechanical, Electronic and Control Engineering, Beijing Jiaotong University, Beijing 100044, China

² Guangdong Provincial Key Lab of Robotics and Intelligent System, Shenzhen Institute of Advanced Technology, Chinese Academy of Sciences, Shenzhen 518005, China

stiffness. Instead of that, rod-driven continuum robots use flexible rods [21–24]. The push and pull actuation of flexible rods withstand tension and compressive force, and increase the structure's rigidity. To achieve different targets such as DOFs or stiffness, several constraint structures are applied, which range from discrete to continuous. Rigid disks [24, 25], bellows [9] and other compliant sheathes [26] are considered applying non-uniform contact force on the flexible rods. Besides, pure soft materials, wrapping the parallel flexible rods and rigid disks, are fabricated to achieve the balanced performance [27]. This paper conducts simulations and experiments based on our previous designed prototype [24]. The development status of the rod-driven continuum robot can be found in Refs. [24, 27].

In addition, it is necessary to establish mathematical models describing the characteristics of the continuum robot. Kinematic models based on the constant curvature assumption reveal the mapping between the configuration space and actuator space, and the configuration space and task space [1], where the profile of the robot segment is assumed to be a circular arc. However, pure kinematics models ignore the effect of gravity, friction, and external load of the environment. They are not accurate in analyzing robot deformation and motion, especially when the continuum robot interacts with the environment and is subject to out-of-plane external loads. Some researchers made efforts to improve the modeling accuracy by combining the pure kinematics and statics model [28] or virtual work principle [21]. The effect of gravity, friction, and external load is considered in these models.

To precisely acquire the robot shape and motion, not only kinematic parameters such as the actuation rod length but also mechanical parameters such as the elastic force, external loading, rod friction, and contact force must be characterized in the mathematical model. Several non-constant curvature approaches have been proposed to improve the modeling accuracy of continuum robots, which can be divided into Cosserat rod theory models [29–32], 3D finite element models (FEMs) [33, 34], and pseudo rigid body models (PRBMs) [2, 35]. Approaches based on the 3D FEM have been explored for modeling and controlling continuum and soft robots [33, 34]. This approach has been limited to quasi-static conditions and does not provide geometric insights into the dynamic behavior. The 3-R PRBM [2, 35] based on the equivalence of elastic potential energy uses the characteristic parameters to describe the kinematics and statics of the continuum robot. However, the position error of the robot with multi rod coupling is still large. This is because the characteristic parameters of the 3-R PRBM are optimized through two extreme load conditions, so

its applicability and accuracy are limited. Compared with the FEM and PRBM, the Cosserat rod theory, although sacrificing the computing efficiency, follows a continuous curve, considers external and internal forces, and has achieved higher calculation accuracy. The Cosserat rod theory, usually neglecting the effect of friction, has been widely used in rod-driven continuum robots [29, 30, 36, 37], cable-driven continuum robots [16, 31], and concentric tube robots [38]. For example, the kinetostatics model of a 6-DOF parallel continuum robot (PCR) ignoring the frictions between rods and constrained disks was established by Orekhov et al. [37]. Another kinematic model of tendon-driven continuum robots given by Amanov et al. [16] also neglected the frictions. To exactly model the continuum robot with winding ropes, the internal friction along the rod must be considered. In summary, a mathematical model considering the effect of gravity, friction, and external load is effective to improve the modeling accuracy and is necessary to analyze the designed rod-driven continuum robot. Furthermore, to the best of our knowledge, no generalized kinetostatics model of a rod-driven multi-module and multi-segment continuum robot is analyzed.

In this paper, a general kinetostatic modeling and deformation analysis for rod-driven continuum robots are developed. The contributions of this work include the followings. (1) To analyze the deformation and load characteristics, a generalized kinetostatics model with the consideration of friction is constructed, which can be applied to the rod-driven continuum robot with multi-module and multi-segment. (2) The shape of in-plane deformation for a two-module continuum robot is defined. Taking a bending plane as an example, the tip deformation along the x -axis of the defined four in-plane shapes is analyzed and compared. (3) The designed two-module rod-driven continuum robot with winding ropes was used to verify the established kinetostatics model.

The paper is organized as follows. The kinetostatics model based on Cosserat rod theory with the consideration of internal friction considered is presented in Section 2, while Section 3 shows the rod-driven two-module continuum robot with winding ropes. Section 4 analyzes the results of simulation and experiment with the conclusions summarized in Section 5.

2 Kinetostatic Modeling of a Multi-Module Continuum Robot

A generalized kinetostatics model based on Cosserat rod theory is established to describe the characteristics of the rod-driven continuum manipulator with multi-module and multi-segment.

The coordinate system is defined as follows:

Table 1 Nomenclature

Symbol	Definition
w, i, j	Module $w, w = 1, 2, \dots, W$; Disk or segment $i, i = e$ denotes end disk of each module; j th actuation rod ($j = 1, 2, 3$)
$O_{wb}-X_{wb}Y_{wb}Z_{wb}, O_{we}-X_{we}Y_{we}Z_{we}, O_{wi}-X_{wi}Y_{wi}Z_{wi}$	Base disk, end disk, and intermediate disk coordinate of module w
Disk_{wi}	i th intermediate disk of module $w. i = e$ means end disk
$\text{Rod}_{\bar{w}ej}$	j th actuation rod connected with end disk e of module \bar{w}
RodC	Central backbone rod
Seg_{wi}	i th segment of module w is between $\text{Disk}_{w(i-1)}$ and Disk_{wi}
$A_{\bar{w}ej,wi}$	Connection point of $\text{Rod}_{\bar{w}ej}$ and Disk_{wi}
$A_{\bar{w}ej,b}$	Connection point of $\text{Rod}_{\bar{w}ej}$ and base disk
$B_{\bar{w}ej,wi}$	Connection point of Disk_{wi} and spring which provides force for winding rope of $\text{Rod}_{\bar{w}ej}$
$B_{\bar{w}ej,b}$	Connection point of base disk and spring which is on the same branch as $\text{Rod}_{\bar{w}ej}$
$S_{\bar{w}ej,wi}$	Arc length of $\text{Rod}_{\bar{w}ej}$ or RodC from $A_{\bar{w}ej,b}$ to $A_{\bar{w}ej,wi}$
$r_{\bar{w}ej,b}$	Position vector of denoted in $O_{wb}-X_{wb}Y_{wb}Z_{wb}$
$r_{\text{spring},\bar{w}ej,b}$	Position vector of denoted in $O_{wb}-X_{wb}Y_{wb}Z_{wb}$
$w = [1, W]$	Force and moment constraint on $A_{\bar{w}ej,wi}$ of $\text{Rod}_{\bar{w}ej}$
$\bar{w} = [w, W]$	Force and moment constraint on O_{wi} of RodC
$n_{\bar{w}ej,wi}^+, m_{\bar{w}ej,wi}^+, n_{\bar{w}ej,wi}^-, m_{\bar{w}ej,wi}^-$	Pulling force on $B_{\bar{w}ej,wi}$ of spring
$n_{wic}^+, m_{wic}^+, n_{wic}^-, m_{wic}^-$	Friction on $A_{\bar{w}ej,wi}$ provided by winding ropes
$F_{\bar{w}ej,wi}^+, F_{\bar{w}ej,wi}^-$	Position and orientation on O_{wi} of RodC denoted in $O_{wb}-X_{wb}Y_{wb}Z_{wb}$
$f_{\bar{w}ej,wi}$	Position and orientation on $A_{\bar{w}ej,wi}$ of $\text{Rod}_{\bar{w}ej}$ denoted in $O_{wb}-X_{wb}Y_{wb}Z_{wb}$
p_{wic}, R_{wic}	Position of $B_{\bar{w}ej,wi}$ denoted in $O_{wb}-X_{wb}Y_{wb}Z_{wb}$
$p_{\bar{w}ej,wi}, R_{\bar{w}ej,wi}$	
$p_{\text{spring},\bar{w}ej,wi}$	

For the intermediate disks, the internal forces and moments of rods undergo a step change when they pass through a disk.

Superscript (+) denotes constraints of Disk_{wi} applied by Seg_{wi} . Superscript (−) denotes constraints of Disk_{wi} applied by $\text{Seg}_{w(i+1)}$.

The base disk coordinate system $\{wb\} = \{X_b, Y_b, Z_b\}$ is located on the base disks. Its origin is the center of the base disk, X_b points from the origin to the first actuation rod, and Z_b is perpendicular to the disk surface.

The end disk coordinate system $\{we\} = \{X_e, Y_e, Z_e\}$ is located on the end disks. Its origin is the center of the end disk, X_e points from the origin to the first actuation rod, and Z_e is perpendicular to the disk surface.

The global coordinate system $\{g\} = \{X_g, Y_g, Z_g\}$ is fixed, and its position coincides with coordinate system $\{wb\}$.

The intermediate disk coordinate system $\{wi\} = \{X_i, Y_i, Z_i\}$ is located on the intermediate disks.

The nomenclature for describing the modeling parameters is shown in Table 1.

The general constraints on disks and rods of a continuum robot with multi-module and multi-segment are shown in Figure 1. Figure 1 (b1) and (c1), Figure 1 (b2) and (c2), and Figure 1 (d1)—(d3) give the detailed constraints on Disk_{wN} , Disk_{wi} and rods, respectively. The forces and moments on each disk should be statically balanced. Boundary values on each rod are applied to the differential equation system. As shown in the overview (Figure 1 (a)), the continuum robot is composed of one central backbone, two adjacent modules, three actuation rods and N disks for each module. Three actuation rods of Module \bar{w} pass through all disks

of Module w . Seg_{wN} is located between Disk_{wN} and Disk_{wi} . All actuation rods for all segments are calculated by the Cosserat rod mechanics. Point A is the connecting point between the actuation rod and disk. Point B is the connecting point between the spring and disk. As shown in the subgraph of Figure 1, all forces and moments on the disks have the same magnitude and opposite direction as those on the rod. The frictions shown as brown arrows and text are not applied to $\text{Rod}_{w\bar{e}j}$ in Disk_{wN} . The springs shown as blue symbols are connected to Disk_{wN} and Disk_{wi} . Detailed explanations for the symbols and letters in Figure 1 can be found in Table 1.

2.1 Cosserat Rod Differential Equation

To describe the deformation of a rod-driven continuum robot taking account of rod elasticity, friction, gravity, and external load, Cosserat rod theory is used to construct the kinostatics model.

Each point on the backbone is denoted by position $p(s) \in \mathbb{R}^3$ and orientation $R(s) \in SO(3)$ with respect to arc length s , which are deduced as follows:

$$\begin{aligned}\dot{R}(s) &= R(s)\hat{u}^I(s), \\ \dot{p}(s) &= R(s)v^I(s),\end{aligned}\quad (1)$$

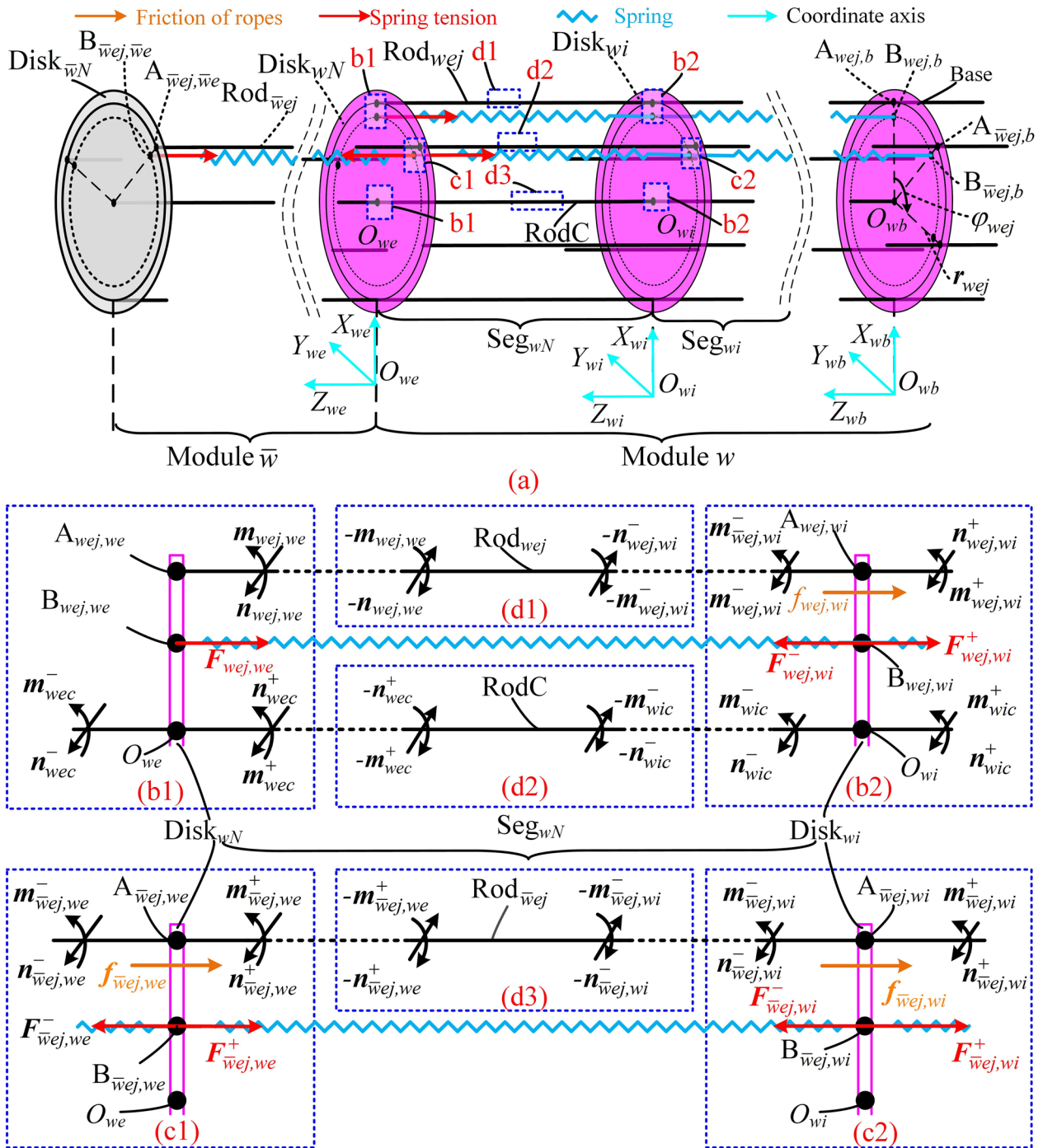


Figure 1 General constraint on disks and rods of continuum robot with multi-module and multi-segment: **a** Overview, **b1–c1** Constraint on Disk_{wN} , **b2–c2** Constraint on Disk_{wi} , **d1–d3** Boundary value on each rod

$\mathbf{v}^l(s)$ and $\mathbf{u}^l(s)$ are kinematics variables, $\hat{\mathbf{u}}^l(s)$ is the skew symmetric matrix of $\mathbf{u}^l(s)$, $\dot{\mathbf{p}}(s)$ and $\dot{\mathbf{R}}(s)$ are the derivative with respect to arc length s .

The internal force $\mathbf{n}(s)$ and moment $\mathbf{m}(s)$ along arc length s are obtained by

$$\begin{aligned} \dot{\mathbf{n}}(s) &= -\mathbf{f}(s), \\ \dot{\mathbf{m}}(s) &= -\dot{\mathbf{p}}(s) \times \mathbf{n}(s) - \mathbf{l}(s), \end{aligned} \quad (2)$$

where $\mathbf{f}(s)$ and $\mathbf{l}(s)$ are the distribution force and moment along the rod, respectively. Considering gravitational

potential energy, $f(s) = \rho A g e_g$, $l(s) = 0$, ρ is the material density, A is the cross area of the rod, g is gravitational acceleration, and e_g is the direction vector of gravity expressed in the global frame.

Linear constitutive laws are assumed to relate the kinematics variables to material strains. The explicit equations can be denoted by

$$\begin{aligned} n(s) &= R(s) K_{se} (v^l(s) - v^l(0)), \\ m(s) &= R(s) K_{bt} (u^l(s) - u^l(0)). \end{aligned} \quad (3)$$

The stiffness matrix for shear and extension is $K_{se} = \text{diag}(AG, AG, AE)$, the matrix for bending and torsion is $K_{bt} = \text{diag}(EI, EI, JG)$, E is the Young's modulus of the flexible rod, G is the shear modulus, and I is the second moment of the area. J is the polar area moment.

2.2 Multi-Rod Boundary Constraints

If the robot only has one module, it is unnecessary to consider the coupling effect of other modules. However, if the robot consists of multiple modules, the module closer to the actuation motor is more affected by the following modules. Therefore, a generalized boundary constraint equation with multiple modules and multiple segments is constructed here.

It is assumed that the robot has a total of W modules represented by parameter w , whose intermediate disks and end disks can be referred to as the constraint disks. As shown in Figure 1, the force and moment in the disks and rods of module $w \in [1, W]$ are analyzed. The same analysis is made for module $\bar{w} \in [w, W]$. If module w is the last module of the robot, then $\bar{w} = w = W$. Each module contains a base disk, several intermediate

disks, an end disk and three actuation rods. The continuum robot with W modules has W end disks, several intermediate disks and a base disk. The end disk of module w can be viewed as the base disk of module $w+1$. The central backbone is fixed evenly connected to each constraint disk, whose position and orientation at the junction are the same as those of the constraint disk. Actuation rods are connected to the end disk of module w and slide freely through the intermediate disks without torsion. Therefore, the actuation rods of module w affect the configuration from module 1 to w . Three actuation rods of each module are arranged evenly along the circumferential direction. The angle between the j th actuation rod fixed on the end disk of module:

$$\varphi_{wej} = \frac{2\pi}{3} \left(\frac{w-1}{W} + j - 1 \right). \quad (4)$$

The position vector of actuation rod can be denoted by:

$$r_{wej} = [\cos\varphi_{wej}, \sin\varphi_{wej}, 0]^T. \quad (5)$$

The relative position of flexible rods in constraint disks is consistent with that in base disk, so r_{wej} is used in the following to represent the position of actuation rods in constraint disks relative to $O_{wi} - x_{wi} y_{wi} z_{wi}$.

Constraints are different due to the coupling effect of each module, which are classified into two conditions: one is the constraint equations of end disks. The other is the constraints of the intermediate disks.

Equations of end disks on module $w \in [1, W]$ are derived as Eqs. (6) and (7), where \bar{w} belongs to $[w+1, W]$ if $w = W$, then $\bar{w} = w$. The force and moment are shown in Figure 1(b1)–(c1). $\mathbf{CoF}_{we}(L)$ and $\mathbf{CoM}_{we}(L)$ are the force and moment constraints on the end disks with rod length L .

$$\mathbf{CoF}_{we}(L) = \sum_{j=1}^3 \mathbf{n}_{wej,we}^+ + \mathbf{n}_{wec}^+ + \text{sgn}(W-w) \left(\sum_{\bar{w}=w+1}^W \sum_{j=1}^3 (\mathbf{n}_{\bar{w}ej,we}^+ - \mathbf{n}_{\bar{w}ej,we}^-) - \mathbf{n}_{wec}^- \right) - \mathbf{F}_{wi} = 0, \quad (6)$$

$$\mathbf{CoM}_{we}(L) = \sum_{j=1}^3 \mathbf{p}_{wej,we} \times \mathbf{n}_{wej,we}^+ + \mathbf{m}_{wej,we}^+ + \mathbf{p}_{wec} \times (\mathbf{n}_{wec}^+ - \mathbf{F}_{wi}) + \mathbf{m}_{wec}^+ - \mathbf{M}_{wi} + \mathbf{C}_e = 0, \quad (7)$$

where

$$\mathbf{C}_e = \text{sgn}(W-w) \left\{ \sum_{\bar{w}=w+1}^W \sum_{j=1}^3 [\mathbf{p}_{\bar{w}ej,we} \times (\mathbf{n}_{\bar{w}ej,we}^+ - \mathbf{n}_{\bar{w}ej,we}^-) + \mathbf{m}_{\bar{w}ej,we}^+ - \mathbf{m}_{\bar{w}ej,we}^-] + \mathbf{p}_{wec} \times (-\mathbf{n}_{wec}^-) - \mathbf{m}_{wec}^- \right\} = 0.$$

The equations of the intermediate disks on module $w \in [1, W]$ are derived as Eqs. (8) and (9), \bar{w} belongs to $[w, W]$. The force and moment are shown in Figure 1(b2)–(c2). $\mathbf{CoF}_{wi}(\mathbf{L})$ and $\mathbf{CoM}_{wi}(\mathbf{L})$ are the force and moment constraints on the intermediate disks. The sgn function is used to determine whether the end disk e is on the last module. If so, the constraints on the end disks exerted by the actuation rods and the central backbone do not undergo a step change.

$$\mathbf{CoF}_{wi}(\mathbf{L}) = \sum_{\bar{w}=w}^W \sum_{j=1}^3 (\mathbf{n}_{\bar{w}ej,wi}^+ - \mathbf{n}_{\bar{w}ej,wi}^-) + \mathbf{n}_{wic}^+ - \mathbf{n}_{wic}^- - \mathbf{F}_{wi} = 0, \quad (8)$$

$$\begin{aligned} \mathbf{CoM}_{wi}(\mathbf{L}) = & \sum_{\bar{w}=w}^W \sum_{j=1}^3 [\mathbf{p}_{\bar{w}ej,wi} \times (\mathbf{n}_{\bar{w}ej,wi}^+ - \mathbf{n}_{\bar{w}ej,wi}^-) \\ & + \mathbf{m}_{\bar{w}ej,wi}^+ - \mathbf{m}_{\bar{w}ej,wi}^-] + \mathbf{p}_{wic} \\ & \times (\mathbf{n}_{wic}^+ - \mathbf{n}_{wic}^- - \mathbf{F}_{wi}) \\ & + \mathbf{m}_{wic}^+ - \mathbf{m}_{wic}^- - \mathbf{M}_{wi} = 0. \end{aligned} \quad (9)$$

The constraint disk not only provides force and moment constraints for actuation and central rods but also provides geometric constraints, which makes the motion of actuation rods not independent. The following conditions for all rods of module \bar{w} connected to disk i of module w should be satisfied.

$$\begin{aligned} [\log(\mathbf{R}_{wic}^T \mathbf{R}_{\bar{w}ej,wi})^\vee]_{xy} &= 0, \\ \mathbf{R}_{wic}^T (\mathbf{p}_{\bar{w}ej,wi} - \mathbf{p}_{wic}) - \mathbf{r}_{wej} &= 0, \end{aligned} \quad (10)$$

where $\bar{w} \in [w, W]$ and all rods $j=1, 2, 3$ of module \bar{w} should satisfy the constraints, $\mathbf{R} = \mathbf{R}_{wic}^T \mathbf{R}_{\bar{w}ej,wi}$ transforms the orientation expressed in the global system into that expressed in the local system, $\log(\cdot)$ is the matrix natural logarithm, which maps $SO(3)$ to $so(3)$, the operator maps $so(3)$ to \mathbf{R}^3 , and the expression $(\cdot)_{xy}$ means the projection of the x and y -axis relative to $O_{wi}-X_{wi}Y_{wi}Z_{wi}$.

2.3 Multi-Rod Boundary Constraints with Internal Friction Considered

Taking the spring tension and winding rope friction into account. The force and moment constraint equations can be expressed as follows.

The equations of the end disk on module $w \in [1, W]$ are derived as Eqs. (11) and (12), where \bar{w} belongs to $[w+1, W]$, if $w = W$, then $\bar{w} = w$. The spring tension and friction are shown in Figure 1(b1)–(c1). $\mathbf{CoF}_{we}(\mathbf{L}, \text{Spring})$ and $\mathbf{CoM}_{we}(\mathbf{L}, \text{Spring})$ are the constraint equations after actuating the spring.

$$\begin{aligned} \mathbf{CoF}_{we}(\mathbf{L}, \text{Spring}) &= \mathbf{CoF}_{we}(\mathbf{L}) + \text{sgn}(W - w) \sum_{\bar{w}=w+1}^W \\ & \sum_{j=1}^3 (\mathbf{F}_{\bar{w}ej,we}^+ - \mathbf{F}_{\bar{w}ej,we}^- + \mathbf{f}_{\bar{w}ej,we}) + \sum_{j=1}^3 \mathbf{F}_{wej,we}^+ = 0, \end{aligned} \quad (11)$$

$$\begin{aligned} \mathbf{CoM}_{we}(\mathbf{L}, \text{Spring}) &= \mathbf{CoM}_{we}(\mathbf{L}) + \sum_{j=1}^3 \mathbf{p}_{spring,wej,we} \\ & \times \mathbf{F}_{wej,we}^+ + \mathbf{C}_e = 0, \end{aligned} \quad (12)$$

where

$$\begin{aligned} \mathbf{C}_e &= \text{sgn}(W - w) \sum_{\bar{w}=w+1}^W \sum_{j=1}^3 [\mathbf{p}_{spring,\bar{w}ej,we} \times (\mathbf{F}_{\bar{w}ej,we}^+ - \mathbf{F}_{\bar{w}ej,we}^-) \\ & + \mathbf{p}_{\bar{w}ej,we} \times \mathbf{f}_{\bar{w}ej,we}] = 0. \end{aligned}$$

The equations of the intermediate disks on module $w \in [1, W]$ are shown as Eqs. (13) and (14), \bar{w} belongs to $[w, W]$. The spring tension and friction are shown in Figure 1(b2)–(c2). $\mathbf{CoF}_{wi}(\mathbf{L}, \text{Spring})$ and $\mathbf{CoM}_{wi}(\mathbf{L}, \text{Spring})$ are the constraint equations on the intermediate disks.

It should be noted that the winding ropes only influence the force and moment constraints, and have no impact on the geometric configuration of each disk. The constraint Eq. (10) stays the same.

$$\begin{aligned} \mathbf{CoF}_{wi}(\mathbf{L}, \text{Spring}) &= \mathbf{CoF}_{wi}(\mathbf{L}) + \sum_{\bar{w}=w}^W \sum_{j=1}^3 (\mathbf{F}_{\bar{w}ej,wi}^+ - \mathbf{F}_{\bar{w}ej,wi}^- + \mathbf{f}_{\bar{w}ej,wi}) = 0, \end{aligned} \quad (13)$$

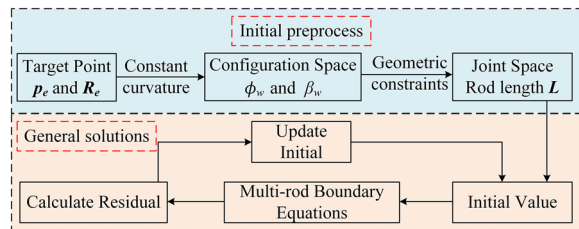
$$\begin{aligned} \mathbf{CoM}_{wi}(\mathbf{L}, \text{Spring}) &= \mathbf{CoM}_{wi}(\mathbf{L}, \text{Spring}) \\ & + \sum_{\bar{w}=w}^W \sum_{j=1}^3 [\mathbf{p}_{\bar{w}ej,wi} \times \mathbf{f}_{\bar{w}ej,wi} + \mathbf{p}_{spring,\bar{w}ej,wi} \\ & \times (\mathbf{F}_{\bar{w}ej,wi}^+ - \mathbf{F}_{\bar{w}ej,wi}^-)] = 0. \end{aligned} \quad (14)$$

2.4 Numerical Solution Method

The unknown parameters for one segment are shown in Table 2. The rotation angle $\gamma_{\bar{w}ej}$ of each actuation rod and arc length $s_{\bar{w}ej-wi}$ of the adjacent disk are unknown, and the axis torque $\mathbf{m}_{\bar{w}ej,wb}|_z$ is zero since the connection between actuation rods and disks is torsionless. The intermediate disks are equally spaced fixed with central backbone, so each integral interval of each differential equation system is determined. But the

Table 2 Unknown parameters for numerical solution

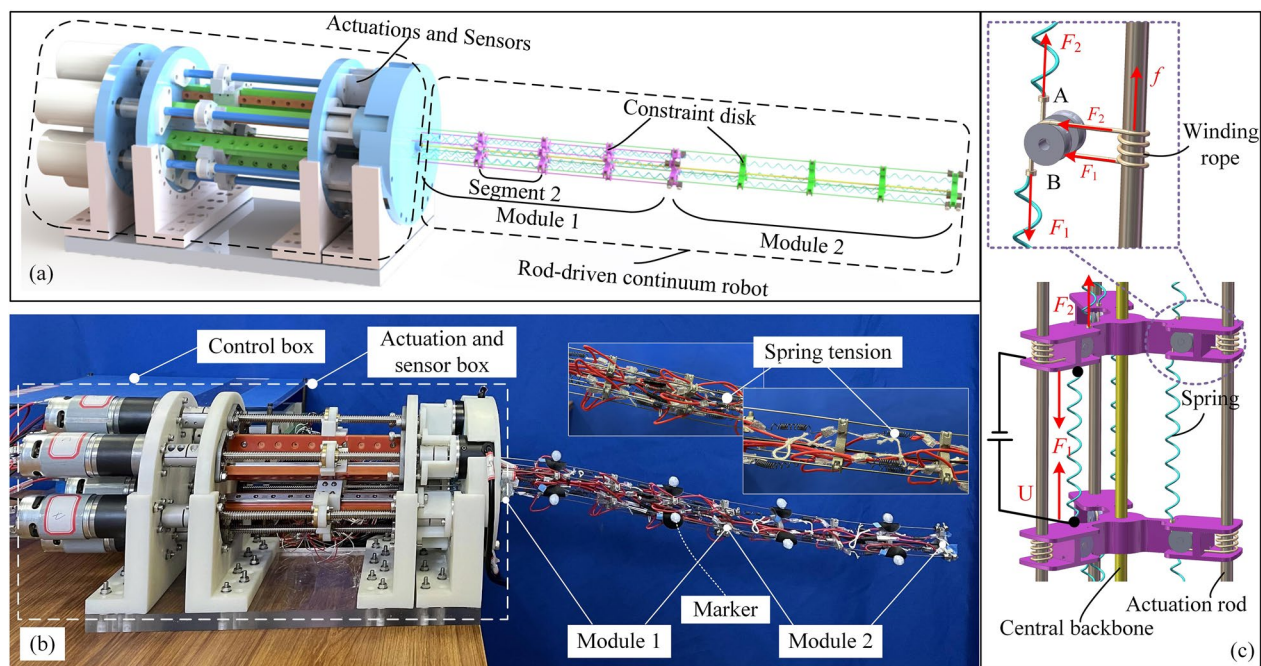
Rod	Unknown parameters
Central rod	$[n_{wec}; m_{wec}]_{6 \times 1}$
Actuation rod on base disks	$[n_{wej,wb}; m_{wej,wb} _{x,y}]_{5 \times 1}$ γ_{wej}
Actuation rod on intermediate	$[n_{wej,wi}; m_{wej,wi} _{x,y}]_{5 \times 1}$ s_{wej_wi}

**Figure 2** Solution to the established model with the preprocessed initial values

convergent solution for lots of initial unknowns, a pre-processing method based on the constant curvature assumptions is adopted to find the initial guess. The solving process is presented in Figure 2.

3 Two-Module Continuum Robot with Winding Ropes

The robot system consists of an actuation module, sensors, and a two-module continuum manipulator, as shown in Figure 3(a). The robot prototype was manufactured to verify the established model, as shown in Figure 3(b). Figure 3(c) presents the detailed structured for one segment with winding ropes. The friction can be divided into the internal force between the rod and constraint disk, and the friction between the rope and rod. The winding rope is tightened due to tension force F_1 and F_2 for each intermediate disk. Thus, the friction between the constraint disk and rod is increased. The detailed designed description and variable stiffness analysis can

**Figure 3** Rod-driven two-module continuum robot system: **a** Structure design of the robot system, **b** Experimental prototype, **c** Structure of one segment with winding ropes

contact force and moment on disks need to find. The shooting method is applied to get the numerical solution, and the solution convergence should be noticed. As for a 6-DOF PCR [39], the convergent solutions were obtained from an arbitrary initial guess due to the fewer unknowns. As for multi-module continuum robots, the number of unknowns increases by 30 as an intermediate disk is added [37]. In order to get

be referred in our recent research [24]. The deformation analysis of this continuum manipulator with the consideration of internal friction will be conducted in this paper.

The length and diameter of the whole manipulator are 480 mm and 36 mm, respectively. The diameter of the central and actuation rods (superelastic NiTi alloy) is 1.5 mm and 1 mm, respectively. The elastic modulus

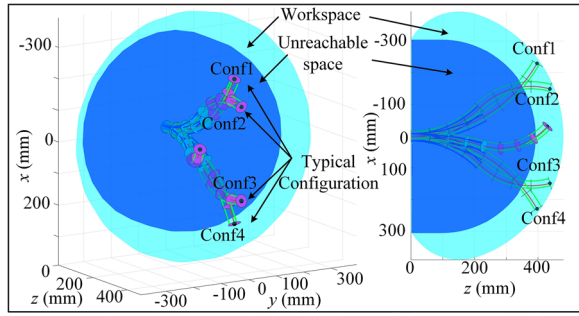


Figure 4 Workspace of the two-module rod-driven continuum robot, and typical configurations

and density of the NiTi rod are 150 GPa and 6.8 g/cm^3 , respectively. The equivalent friction coefficient is taken as 1.5 which is referred from Ref. [24]. The configurations are measured by the attached marker along the manipulator. The MotionAnalysis capture equipment (resolution 0.1 mm) is used to capture the marker motion.

4 Experiments and Simulations

4.1 Workspace of Two-Module Continuum Robot

The configuration of module w is denoted by $[\phi_w, \beta_w]$, where $\phi_w \in [0, 2\pi]$ and $\beta_w \in [0, \pi/2]$. ϕ_w represents the angle of bending plane. β_w represents the bending angle of each module. A two-module continuum robot is simply denoted by the quadruplets of angles $[\phi_1, \beta_1, \phi_2, \beta_2]$. A series of configuration within the angle range is generated. Then the tip position is calculated for each of them.

The shape of the reachable workspace of the two-module continuum robot is similar to a shell, as shown in Figure 4. The inner space of the shell is the unreachable space. The workspace provides a theoretical guide when operating tasks. Conf1, Conf2, Conf3 and Conf4 are chosen to analyze their deformation under external loads. The parameters of the configuration space of these four configurations during the initial preprocessing can be expressed by $[\phi_1, \beta_1, \phi_2, \beta_2]$. Conf1 and Conf4 with $[\pi/6, \pi, \pi/6, \pi]$ and $[\pi/6, 0, \pi/6, 0]$, respectively, are C-shaped bending, and Conf2 and Conf3 with $[\pi/5, \pi, \pi/4, 0]$ and $[\pi/5, 0, \pi/4, \pi]$, respectively, are S-shaped bending.

4.2 Comparative Simulations of in-Plane Deformation under External Load

The shapes of in-plane deformation under external load are defined in Table 3. Different shapes exhibit different deformation characteristics when an external force is applied, which are defined as S1, S2, C1, and C2. All in-plane shapes are considered with the bending plane

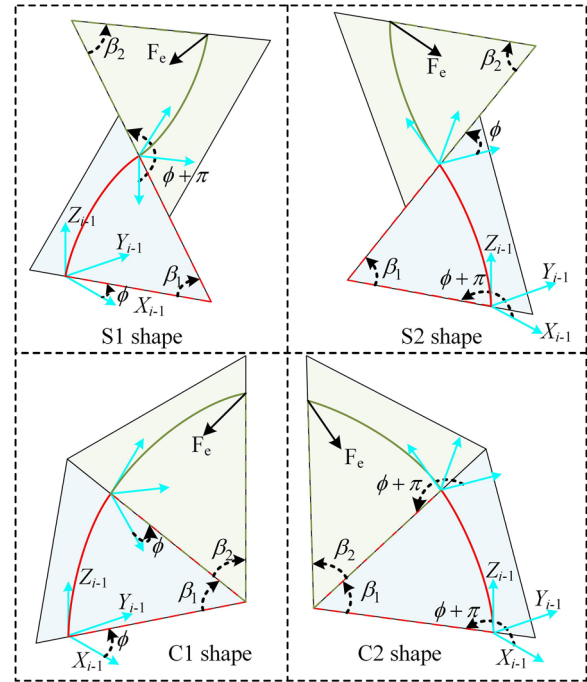


Figure 5 Detailed descriptions of S1, S2, C1, and C2

angle ϕ_w ranging from $-\pi/2$ to $\pi/2$. All external forces are assumed to be applied in the same plane. The detailed descriptions of these four shapes are shown in Figure 5.

Taking the angle of the bending plane $\phi = 0$ into consideration, external weight $F_e = 100 \text{ g}$ along x -axis is applied on the end disk for the four types of shape. Different total bending angles ranging from 0 to $\pi/4$ are used as the initial guess to get the numerical solutions. The final deformation along the x -axis is compared, as shown in Figure 6. The load capacity of C1 and C2 is generally larger than that of S1 and S2. Furthermore, the stiffness of C1 and C2 increases with the increase of the total bending angle of the two modules. Especially, the stiffness of these two shapes has dramatic rise when the bending angle is nearly on the workspace boundary. The stiffness of S1 and S2 increases with the increase of the bending angle of the first module and the decrease of the bending angle of the second module.

Table 3 In-plane deformation under external loads

Type	Angle of bending plane ($\phi \in [-\pi/2, \pi/2]$)		Bending angle
S1 shape	$\phi_1 = \phi$	$\phi_2 = \phi + \pi$	$\beta_1, \beta_2 \in [0, \pi/4]$
S2 shape	$\phi_1 = \phi + \pi$	$\phi_2 = \phi$	$\beta_1, \beta_2 \in [0, \pi/4]$
C1 shape	$\phi_1 = \phi$	$\phi_2 = \phi$	$\beta_1, \beta_2 \in [0, \pi/4]$
C2 shape	$\phi_1 = \phi + \pi$	$\phi_2 = \phi + \pi$	$\beta_1, \beta_2 \in [0, \pi/4]$

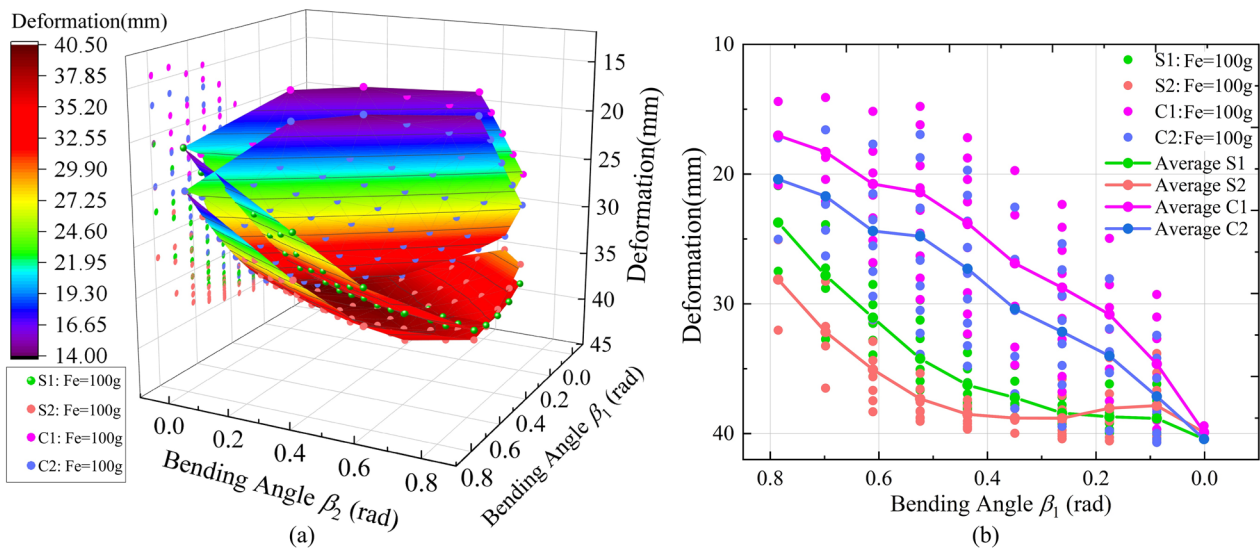


Figure 6 Deformation comparison of S1, S2, C1, and C2 shape under external weight $F_e = 100$ g: **a** Deformation distribution of in-plane bending, **b** Average deformation comparison

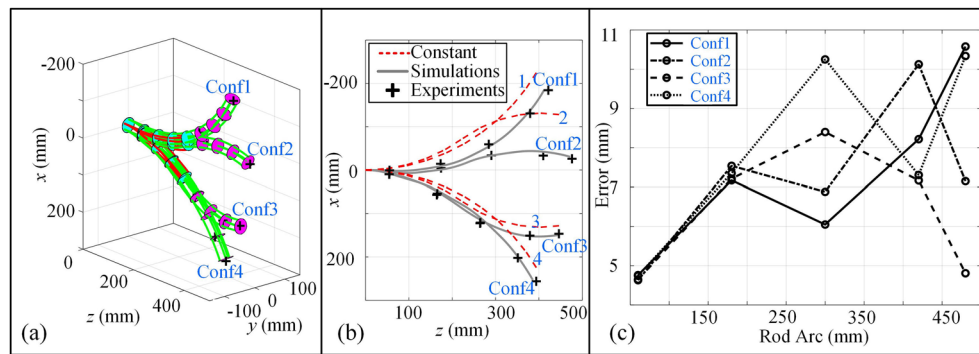


Figure 7 Simulations and experiments of different configurations: **a** Simulation configuration of Conf1, Conf2, Conf3, and Conf4, **b** Deformation without loads, **c** Errors along rod length between established model and experimental results

4.3 Deformation Analysis without External Load

Experimental and simulation deformations of the Conf1, Conf2, Conf3 and Conf4 under an external load (weight 100 g, along the positive x -axis) are analyzed.

Figure 7(a) shows these configurations solved by the theoretical model. Figure 7(b) compares the simulation results and experimental data. The red dashed line 1, 2, 3, and 4 are calculated based on the constant curvature during the initial process shown in Figure 2. These preprocessing configurations are used to obtain Conf1, Conf2, Conf3, and Conf4, respectively. The final results obtained from preprocessed initial values are quite different from the experiments and simulations. Therefore, the constant curvature kinematics are not accurate enough for the case of an external load. Figure 7(c)

shows that the error along the manipulator is relatively small, which means that the simulation results are consistent with the experiment. The maximum error of the end disk does not exceed 11 mm, and the error relative to the overall length is 2.29%.

4.4 Deformation of Different Configurations under the Same External Load

Under the same external load, different configurations have different deformation characteristics. Figure 8(a) and (b) show the simulation and experimental deformations of Conf1, Conf2, Conf3, and Conf4 under 100 g at end disk. Figure 8(c) and (d) show the deformation of Conf1, Conf2, Conf3, and Conf4 under 200 g at the end disk. The bending directions of the first module of

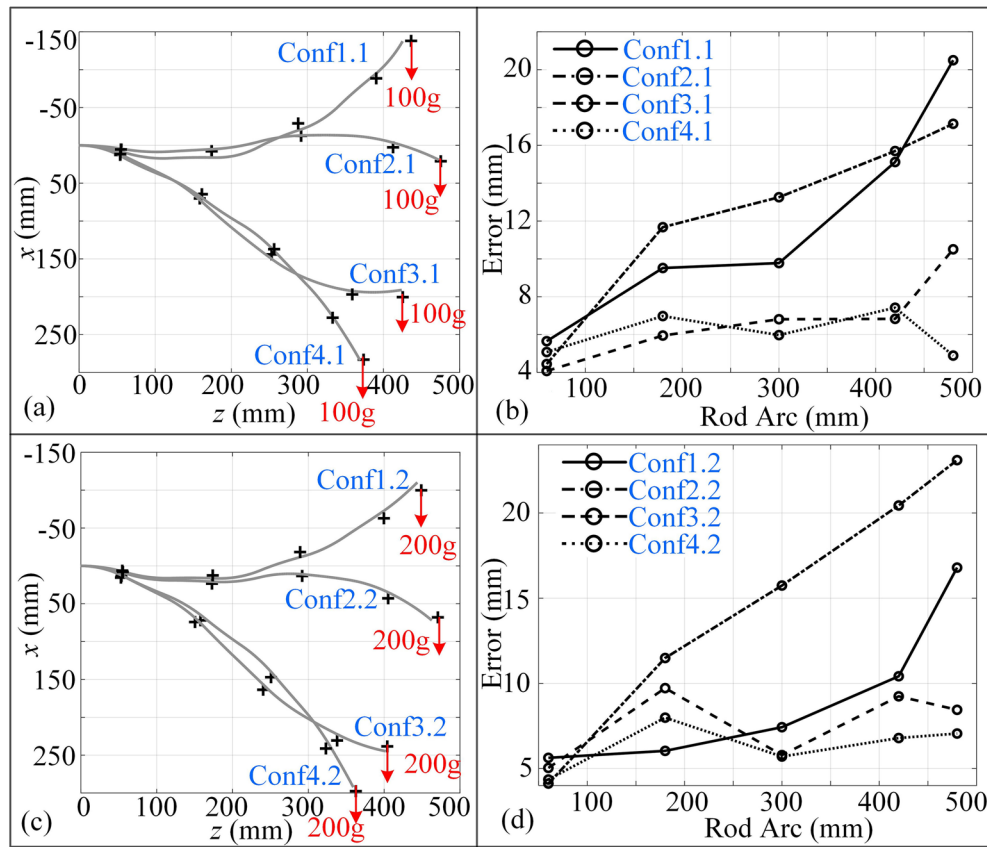


Figure 8 Effects of different configurations under 100 g and 200 g respectively: **a** Deformation under the 100 g, **b** Error along arc with 100 g, **c** Deformation under 200 g, **d** Errors along arc with 200 g

Conf1.1, Conf1.2, Conf2.1 and Conf2.2 and the second module of Conf3.1 and Conf3.2 are opposite to the load direction. As shown in Figure 8(a) and (c), the experimental curves of Conf1.1 and Conf1.2 are not smoother than those of the others due to the opposite loads with respect to the bending direction. In addition, regardless of whether the external load direction is opposite or the same as the bending direction of the first module, the S-shaped configurations produce greater bending, such as groups Conf2.1 and Conf3.1 compared with groups Conf1.1 and Conf4.1 or groups Conf2.2 and Conf3.2 compared with groups Conf1.2 and Conf4.2, respectively. Furthermore, a configuration such as Conf4.2 with the same module direction and load direction has greater bending resistance than the others. The configuration errors of the first module with the same bending and load direction are relatively small, 2.08% and 1.7%, as shown in Figure 8(b) and (d). The configuration errors of the first module with the bending direction opposite to the load are 4.17% and 4.69%.

4.5 Deformation of the Same Configuration with Different External Loads

Figure 9(a) and (c) give the deformation of Conf5 = $[\pi/6, 0, \pi/5, \pi]$ with opposite bending direction module under 150 g, 250 g, -150 g and -250 g loads, and configuration Conf6 = $[\pi/10, \pi, \pi/10, \pi]$ with the same bending direction module under 150 g, -150 g and -250 g loads. Figure 9(b) and (d) show the corresponding errors. The deformations without external load are Conf5 and Conf6. As the external load increases, the deformation of the robot becomes greater. The total deformation of Conf5.1 and Conf5.2 is greater than that of Conf5.3 and Conf5.4, but the end disk errors of Conf5.3 and Conf5.4 are larger than others. Furthermore, the curvature of the second module of Conf5 gradually decreases under a positive load so that the degree of the S-shape decreases, as in Conf5.1 and Conf5.2. The curvature of the second module gradually increases under the negative load so that the degree of the S-shape increases, such as Conf5.3 and Conf5.4. For Conf6, the first module of Conf6.1 with the bending direction opposite to the load direction produces

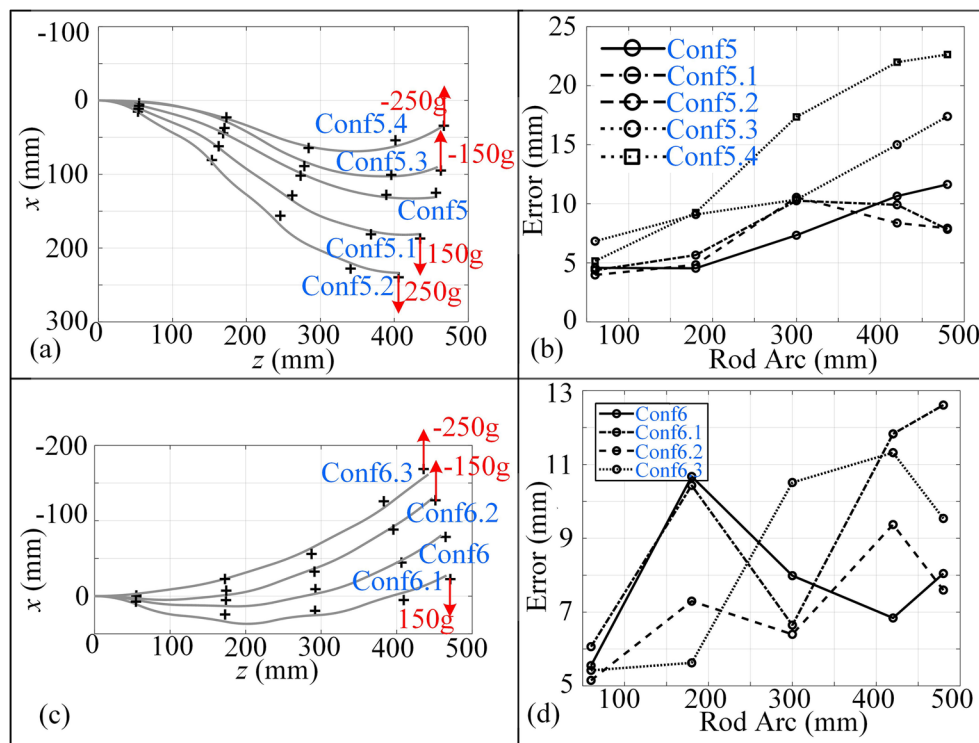


Figure 9 Deformations of Conf5 and Conf6 with different load: **a** Deformation of Conf5 with 150 g, 250 g, - 150 g and - 250 g loads, **b** Errors along rod arc of Conf5, **c** Deformation of Conf6 with 150 g, - 150 g and - 250 g loads, **d** Errors along rod arc of Conf6

a large local deformation, and the end disk error is larger compared with others.

5 Conclusions

This paper can be concluded as the following points.

- (1) A generalized kinetostatics model based on the Cosserat rod theory with friction considered for multi-module and multi-segment continuum robots is established. Several experiments based on a two-module rod-driven continuum robot are conducted to verify the established model.
- (2) The shape of in-plane deformation for two-module continuum robot is defined as C1, C2, S1, and S2. Taking a bending plane as an example, the tip deformation along the x -axis for these shapes with external force applied is analyzed and compared. Generally, the load capacity of C1 and C2 is larger than that of S1 and S2.
- (3) Comparative deformation experiments for different configurations show that the maximum error ratio without external loads between simulations and experiments is no more than 3% (relative to the total length), and it is no more than 4.7% under the exter-

nal load, which occurs in C1 and C2 bending configuration with the opposite load direction.

As for future work, variable stiffness and adaptive motion control method should be developed for further application on detection and maintenance tasks in unstructured environments. Besides, many experiments will be conducted to verify the accuracy of the established model under out-plane external forces. Finally, computation efficiency should be improved for the further real-time motion control.

Acknowledgements

Not applicable.

Author contributions

PW and SG are in charge of the whole trial and wrote the manuscript. XY and XW are in charge of the prototype manufacturing. All authors read and approved the final manuscript.

Author's Information

Peiyi Wang, born in 1995, is currently a PhD candidate at School of Mechanical, Electronic and Control Engineering, Beijing Jiaotong University, China. He received his bachelor's degree from Beijing Jiaotong University, China, in 2018. His research interests include mechanical design and control continuum robot. Xinhua Yang, born in 1999, is currently a PhD candidate at School of Mechanical, Electronic and Control Engineering, Beijing Jiaotong University, China. He received his bachelor's degree from Beijing Jiaotong University, China, in 2021. His research interests include continuum robot and exoskeleton robot. Xiangyang Wang, born in 1995, received his B.E. and PhD degree in mechanical engineering, in 2017 and 2022 respectively, from Beijing Jiaotong University,

China. Currently, he is with Guangdong Provincial Key Lab of Robotics and Intelligent System, Shenzhen Institute of Advanced Technology, Chinese Academy of Sciences. His research interests include mechanical design and control of lower-limb exoskeletons.

Sheng Guo, born in 1972, received his Ph.D. degree from *Beijing Jiaotong University, China*, in 2005. He was a visiting scholar at *University of California, Irvine, US*, in 2010 and 2011. Currently, he is a full professor and vice director of *Robotics Institute*, and the dean of *School of Mechanical, Electronic and Control Engineering, Beijing Jiaotong University, China*. His research interests include robotic mechanisms and mechatronics.

Funding

Supported by National Natural Science Foundation of China (Grant No. 51875033), Fundamental Research Funds for the Central Universities of China (Grant No. 2021YJS137).

Availability of Data and Materials

The datasets supporting the conclusions of this article are included within the article.

Declarations

Ethics Approval and Consent to Participate

Not applicable.

Consent for Publication

Not applicable.

Competing Interests

The authors declare no competing financial interests.

Received: 1 June 2022 Revised: 29 April 2023 Accepted: 4 May 2023

Published online: 06 June 2023

References

- [1] R J Webster, B A Jones. Design and kinematic modeling of constant curvature continuum robots: A review. *International Journal of Robotics Research*, 2010, 29(13): 1661-1683.
- [2] S P Huang, D S Meng, Y She, et al. Statics of continuum space manipulators with nonconstant curvature via pseudorigid-body 3r model. *IEEE Access*, 2018, 6: 70854-70865.
- [3] J Barrientos-Diez, X Dong, D Axinte, et al. Real-time kinematics of continuum robots: Modelling and validation. *Robotics and Computer-Integrated Manufacturing*, 2021, 67: 102019.
- [4] X Dong, D Palmer, D Axinte, et al. In-situ repair/maintenance with a continuum robotic machine tool in confined space. *Journal of Manufacturing Processes*, 2019, 38: 313-318.
- [5] M Wang, D Palmer, X Dong, et al. Design and development of a slender dual-structure continuum robot for in-situ aeroengine repair. *Proceedings of the IEEE/RSJ International Conference on Intelligent Robots and Systems (IROS)*, Madrid, Spain, 2018: 5648-5653.
- [6] L Tang, J Huang, L M Zhu, et al. Path tracking of a cable-driven snake robot with a two-level motion planning method. *IEEE/ASME Transactions on Mechatronics*, 2019, 24(3): 935-946.
- [7] L Tang, J Wang, Y Zheng, et al. Design of a cable-driven hyper-redundant robot with experimental validation. *International Journal of Advanced Robotic Systems*, 2017, 14(5): 1-12.
- [8] S T Liu, Z X Yang, Z J Zhu, et al. Development of a dexterous continuum manipulator for exploration and inspection in confined spaces. *Industrial Robot-An International Journal*, 2016, 43(3): 284-295.
- [9] K Xu, J R Zhao, M X Fu. Development of the sjtu unfoldable robotic system (surs) for single port laparoscopy. *IEEE/ASME Transactions on Mechatronics*, 2015, 20(5): 2133-2145.
- [10] H B Gilbert, J Neimat, R J Webster. Concentric tube robots as steerable needles: Achieving follow-the-leader deployment. *IEEE Transactions on Robotics*, 2015, 31(2): 246-258.
- [11] M Cianchetti, T Ranzani, G Gerboni, et al. Stiff-flop surgical manipulator: Mechanical design and experimental characterization of the single module. *Proceedings of the IEEE/RSJ International Conference on Intelligent Robots and Systems (IROS)*, Tokyo, Japan, 2013: 3576-3581.
- [12] C Wang, C G Frazelle, J R Wagner, et al. A discrete-jointed robot model based control strategy for spatial continuum manipulators. *Proceedings of the IECON 2020 The 46th Annual Conference of the IEEE Industrial Electronics Society*, Singapore, 2020: 543-549.
- [13] R Kang, D T Branson, T Zheng, et al. Design, modeling and control of a pneumatically actuated manipulator inspired by biological continuum structures. *Bioinspiration & Biomimetics*, 2013, 8(3): 036008.
- [14] R J Webster, J M Romano, N J Cowan. Mechanics of precurved-tube continuum robots. *IEEE Transactions on Robotics*, 2009, 25(1): 67-78.
- [15] K Oliver-Butler, J A Childs, A Daniel, et al. Concentric push-pull robots: Planar modeling and design. *IEEE Transactions on Robotics*, 2021: 1-15.
- [16] E Amanov, T D Nguyen, J Burgner-Kahrs. Tendon-driven continuum robots with extensible sections-a model-based evaluation of path-following motions. *International Journal of Robotics Research*, 2019, 40(1): 7-23.
- [17] Z Liu, X Zhang, Z Cai, et al. Real-time dynamics of cable-driven continuum robots considering the cable constraint and friction effect. *IEEE Robotics and Automation Letters*, 2021, 6(4): 6235 - 6242.
- [18] D Wei, T Gao, X Mo, et al. Flexible bio-tensegrity manipulator with multi-degree of freedom and variable structure. *Chinese Journal of Mechanical Engineering*, 2020, 33(1): 1-11.
- [19] S Qian, B Zi, W W Shang, et al. A review on cable-driven parallel robots. *Chinese Journal of Mechanical Engineering*, 2018, 31(1): 66.
- [20] E Idà, S Briot, M Caricato. Identification of the inertial parameters of underactuated cable-driven parallel robots. *Mechanism and Machine Theory*, 2022, 167: 104504.
- [21] C Yang, S Geng, I Walker, et al. Geometric constraint-based modeling and analysis of a novel continuum robot with shape memory alloy initiated variable stiffness. *International Journal of Robotics Research*, 2020, 39(14): 1620-1634.
- [22] Y Chen, B Wu, J Jin, et al. A variable curvature model for multi-backbone continuum robots to account for inter-segment coupling and external disturbance. *IEEE Robotics and Automation Letters*, 2021, 6(2): 1590-1597.
- [23] J Yang, C Ren, C Yang, et al. Design of a flexible capture mechanism inspired by sea anemone for non-cooperative targets. *Chinese Journal of Mechanical Engineering*, 2021, 34(1): 1-13.
- [24] P Wang, S Guo, X Wang, et al. Design and analysis of a novel variable stiffness continuum robot with built-in winding-styled ropes. *IEEE Robotics and Automation Letters*, 2022, 7(3): 6375-6382.
- [25] K Xu, N Simaan. An investigation of the intrinsic force sensing capabilities of continuum robots. *IEEE Transactions on Robotics*, 2008, 24(3): 576-587.
- [26] J A Childs, C Rucker. Leveraging geometry to enable high-strength continuum robots. *Frontiers in Robotics and AI*, 2021, 8: 629871-629871.
- [27] P Wang, Z Tang, W Xin, et al. Design and experimental characterization of a push-pull flexible rod-driven soft-bodied robot. *IEEE Robotics and Automation Letters*, 2022, 7(4): 8933-8940.
- [28] H Yuan, L Zhou, W Xu. A comprehensive static model of cable-driven multi-section continuum robots considering friction effect. *Mechanism and Machine Theory*, 2019, 135: 130-149.
- [29] B A Jones, R L Gray, K Turlapati. Three dimensional statics for continuum robotics. *Proceedings of the IEEE/RSJ International Conference on Intelligent Robots and Systems (IROS)*, St. Louis, MO, USA, 2009: 2659-2664.
- [30] C B Black, J Till, C Rucker. Parallel continuum robots: Modeling, analysis, and actuation-based force sensing. *IEEE Transactions on Robotics*, 2018, 34(1): 29-47.
- [31] D C Rucker, R J Webster. Statics and dynamics of continuum robots with general tendon routing and external loading. *IEEE Transactions on Robotics*, 2011, 27(6): 1033-1044.
- [32] F Renda, M Giorelli, M Calisti, et al. Dynamic model of a multibending soft robot arm driven by cables. *IEEE Transactions on Robotics*, 2014, 30(5): 1109-1122.
- [33] F Largilliere, V Verona, E Coevoet, et al. Real-time control of soft-robots using asynchronous finite element modeling. *Proceedings of the IEEE International Conference on Robotics and Automation (ICRA)*, Seattle, WA, USA, 2015: 2550-2555.
- [34] J Bosman, T M Bieze, O Lakhall, et al. Domain decomposition approach for fem quasistatic modeling and control of continuum robots with rigid

vertebras. *Proceedings of the IEEE International Conference on Robotics and Automation (ICRA)*, Seattle, WA, USA, 2015: 4373–4378.

- [35] S Huang, D Meng, X Wang, et al. A 3D static modeling method and experimental verification of continuum robots based on pseudo-rigid body theory. *Proceedings of the IEEE/RSJ International Conference on Intelligent Robots and Systems (IROS)*, Macau, China, 2019: 4672–4677.
- [36] G L Wu, G L Shi. Experimental statics calibration of a multi-constraint parallel continuum robot. *Mechanism and Machine Theory*, 2019, 136: 72–85.
- [37] A L Orekhov, V A Aloj, D C Rucker. Modeling parallel continuum robots with general intermediate constraints. *Proceedings of the IEEE International Conference on Robotics and Automation (ICRA)*, Singapore, 2017: 6142–6149.
- [38] D C Rucker, B A Jones, R J Webster. A geometrically exact model for externally loaded concentric-tube continuum robots. *IEEE Transactions on Robotics*, 2010, 26(5): 769–780.
- [39] C E Bryson, D C Rucker. Toward parallel continuum manipulators. *Proceedings of the IEEE International Conference on Robotics and Automation (ICRA)*, Hong Kong, China, 2014: 778–785.

Submit your manuscript to a SpringerOpen[®] journal and benefit from:

- Convenient online submission
- Rigorous peer review
- Open access: articles freely available online
- High visibility within the field
- Retaining the copyright to your article

Submit your next manuscript at ► [springeropen.com](https://www.springeropen.com)
